CHALMERS
UNIVERSITY OF TECHNOLOGY

Experimental and numerical investigation of cavitation in marine Diesel injectors

International Journal of Heat and Mass Transfer 169 (2021) 120933

Contents lists available at ScienceDirect

International Journal of Heat and Mass Transfer

journal homepage: www.elsevier.com/locate/hmt

Experimental and numerical investigation of cavitation in marine Diesel injectors

Reto Balz [a,b,*], Imre G. Nagy [b,c], German Weisser [b], David Sedarsky [a]

[a] Chalmers University of Technology, Department of Mechanics and Maritime Sciences, Göteborg, Sweden
[b] Winterthur Gas & Diesel Ltd., Winterthur, Switzerland
[c] National Technical University of Athens, School of Naval Architecture and Marine Engineering, Athens, Greece

ARTICLE INFO

Article history:
Received 14 May 2020
Revised 31 October 2020
Accepted 5 December 2020

Keywords:
Fuel injection
Cavitation
In-nozzle flow
CFD
Large marine diesel engine

ABSTRACT

To further increase the efficiency and decrease emissions of large two-stroke marine Diesel engines, the understanding of the fuel injection, spray breakup and the resulting combustion plays a vital role. Investigations have shown that the strongly asymmetrically and eccentrically arranged nozzle bores of the fuel injectors can lead to undesirable spray deflections that provoke increased component temperatures, emissions and fuel consumption. In order to investigate the origin of these spray deviations, transparent nozzles have been used to qualitatively visualize the in-nozzle flow under realistic geometrical and fuel pressure conditions. Three different, 0.75 mm diameter, single-hole nozzle geometries that represent typical geometrical characteristics have been used in cavitating nozzle flow experiments. The optical measurement technique Shadowgraphy has been applied to visualize the in-nozzle flow over the complete fuel injection process. The experiments have been performed with Diesel fuel at a rail pressure of 50 MPa with ambient back-pressure and temperature. Impingement measurements have been executed to compare the nozzle performance and validate CFD simulations using URANS with cavitation modeling in order to provide qualitative and quantitative support to the experimental results. The volume of fluid (VOF) method has been applied to simulate the multiphase flow with High Resolution Interface Capturing (HRIC). The cavitation model is based on a flash-boiling method with rapid heat transfer between the liquid and vapor phases. A Homogeneous Relaxation Model (HRM) has been utilized to describe the rate at which the instantaneous quality, the mass fraction of vapor in a two-phase mixture, will approach its equilibrium value.

The numerical modeling of the cavitation inside the nozzle bore and the evaluated momentum flux have been compared to the experimental findings and show good agreement for the qualitative comparison of the cavitation patterns and differences of less than 6% for the quantitative momentum flux comparison.

1. Introduction

1.1. Background

Large two-stroke marine Diesel engines belong to the most efficient internal combustion engines existing and can reach efficiencies over 55% [1]. To further decrease emissions and increase the overall efficiency, the understanding of the fuel injection plays a crucial role. Development strategies which can maintain highly efficient combustion while reducing pollutant formation require a more granular understanding of the mixture preparation, which is the driving force of in-cylinder combustion.

Due to the large bore of two-stroke marine Diesel engines and a strong swirl motion of the charged air, multiple fuel injectors are used and arranged around the single exhaust valve. As a result, the typical three fuel injectors arranged by 120° have highly eccentrically and asymmetrically arranged nozzle bores. A typical nozzle tip that is mounted on the fuel injector is illustrated in Fig. 1. Note the five-hole nozzle design where all five nozzle bores face a similar direction. This particular nozzle design and the large nozzle bore diameters limit the usability of research focused on small- and medium-sized Diesel engines.

Some of the specific issues that affect fuel injection in large marine Diesel engines have been examined by experiments conducted

* Corresponding author.
E-mail addresses: balz@chalmers.se, reto.balz@wingd.com (R. Balz).

https://doi.org/10.1016/j.ijheatmasstransfer.2021.120933

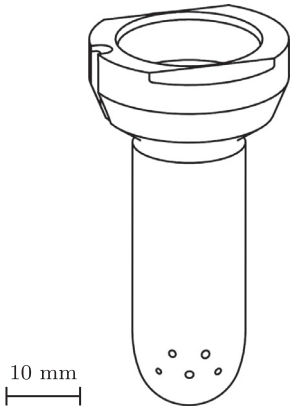

Fig. 1. Illustration of a standard nozzle tip for large two-stroke marine Diesel engine fuel injectors indicating the typically five-hole design of the nozzle bores. Note that the main body diameter is 15 mm and the nozzle bores have diameters around 1 mm. The nozzle tips are exchangeable and directly mounted on the fuel injectors (not depicted).

in the constant-volume Spray and Combustion Chamber (SCC) at Winterthur Gas & Diesel Ltd. (WinGD) [2]. Investigations in the SCC have shown that the asymmetric and eccentric nozzle layout of large two-stroke marine Diesel engine fuel injectors has a significant influence on spray formation [3,4]. Additionally, CFD simulations have shown that inhomogeneous fuel velocity profiles in the nozzle bores induced by geometric cavitation lead to significant spray deflections, especially for eccentrically arranged nozzle bores [5,6].

To further investigate the in-nozzle flow and how it affects the spray morphology of large two-stroke marine Diesel engine injectors, experiments have been performed using transparent nozzles made of polymethyl methacrylate (PMMA). The feasibility of using PMMA as material to visualize in-nozzle flow has been proven by countless work over the last years [7–13]. Although different non-invasive measurement techniques have been proven successful to investigate the in-nozzle flow under real fuel injection conditions, the use of transparent nozzle tips still allows the highest spatial and temporal resolutions, especially compared to x-ray imaging. The flow inside multi-hole marine injectors has previously been studied optically only using transparent models with water at a few atmospheres pressure as working fluid [7,14]. Yang *et al.* [15] provide an up-to-date and detailed review of the experimental non-intrusive investigations of fuel injector phase changing flow. In this study, full-scale nozzle diameters and realistic injection pressures with real Diesel fuel are utilized in order to match set points for WinGD marine Diesel engines. The design of optically transmissive injector inserts provides the possibility of production nozzle geometry duplication while realistic injection pressures can be applied. This allows the acquisition of optical measurements which provide insights for model development and can be used for the validation of cavitation modeling results based on CFD for large marine Diesel engine atomizers.

1.2. In-nozzle cavitation

Cavitation is the process of formation and consequent collapse of gaseous bubbles in a liquid under a local decrease in static pressure. Depending on the topology of the vapor structures in the flow, cavitation occurs in the form of traveling bubbles or vapor pockets, extending over a partial length of the nozzle bore (cloud cavitation and sheet cavitation), or supercavitation, when the vapor region extends over the whole length of the nozzle bore [16,17].

Hydrodynamic cavitation in fuel injectors develops at high injection rates when the pressure drops below the critical level inside the nozzle bore, leading the fuel to evaporate into vapor. Cavitation is reported to improve the spray breakup processes [18–22]. However, undesirable effects on the fuel injection performance may occur, such as flow instabilities, excessive noise generation, and erosion, which can cause damage to the injector and nozzles [23].

To characterize the flow inside the nozzle, the dimensionless discharge coefficient providing the ratio between actual and theoretical discharge through the nozzle bore is used:

$$C_D = \frac{\dot{m}_{actual}}{\dot{m}_{ideal}} \tag{1}$$

where $\dot{m}_{ideal}$ is the theoretical mass flow based on Bernoulli's equation and $\dot{m}_{actual}$ the actual, entropy bounded, mass flow through the atomizer.

2. Experimental methods

2.1. Optically transparent nozzle holder

A transparent nozzle holder (TNH) to be mounted on fuel injectors of large marine Diesel engines has originally been developed at Chalmers University of Technology [24] and proved to cope with fuel pressures in the ranges of large two-stroke marine Diesel engines (50 to 80 MPa rail pressure) for a limited number of injections (usually around 20 to 60 injections before failure). The design uses transparent nozzles made from PMMA. The thermoplastic has a similar optical refractive index to Diesel (1.49 and 1.46 to 1.52 depending on the Diesel mixture, respectively) that allows visualization of the in-nozzle flow without optical distortions due to the round shape of the nozzle bore that otherwise would act as a cylindrical lens. The transparent nozzle is mounted onto the TNH with rigid metallic clamps that apply an external force onto the nozzle to suppress the expansion of the PMMA. This clamping reduces the internal stresses in the PMMA and decreases the failure probability significantly (see [11] for further information). For the optically interesting axis, polished sapphire bricks have been used between the metal clamps and the PMMA nozzle to guarantee maximal optical access while still applying a clamping force on the plastic.

Fig. 2 illustrates the used TNH. The entire setup can be mounted on a typical WinGD injector by using the injector mount (e). The main bore leads the fuel to the PMMA nozzle (k) and the pressure sensor (a). The metallic top-clamps (c) apply force directly to the PMMA nozzle, while the side-clamps (g) provide stability via two polished sapphire bricks (h) to maintain optical access. The PMMA nozzle is also fixed by using two fitting bolts (f) that connect the sensor-body (b) and the main-body (d) together. The depicted transparent nozzle (k) is a single-hole, perpendicular design with a nozzle bore diameter of 0.75 mm. The sensor-body (b) presented in Fig. 2 holds a pressure transducer that allows measuring the fuel pressure in the main bore of the TNH. The used piezo-resistive pressure sensor from Kistler (type 4067C2000) has a natural frequency of over 200 kHz that allows dynamic acquisition of the fuel pressure in the main bore of the nozzles. The pressure sensor allows accurate data acquisition that is necessary to investigate cavitation behavior during the quasi-steady-state injection conditions. It is important that the pressure at the main bore is known during the whole injection process to better understand cavitation fluctuations in the nozzle bore. The measured data has crucial importance as a boundary condition in CFD simulations since fuel injectors usually have significant pressure losses.

2.2. Nozzle geometries

Three different single-hole cylindrical nozzle designs have been chosen based on the realistic five-hole atomizer designs of large

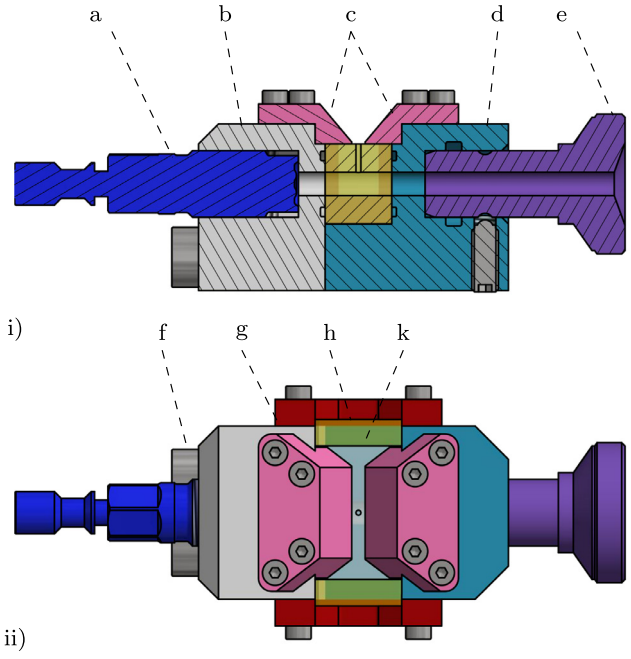

Fig. 2. Sectional view (i) and top view (ii) illustration of the new transparent nozzle holder with pressure sensor (a), sensor-body (b), top-clamps (c), main-body (d), injector mount (e), fitting bolt (f) side-clamp (g), sapphire brick (h) and transparent nozzle (k).

two-stroke marine Diesel engine injectors. This simplification has been chosen to reduce the computational cost for CFD simulations and to reduce the experimental effort. The application of five-hole nozzle bores would complicate the optical access since they are overlapping in the interesting optical axis and, as a result, would limit the information about the in-nozzle flow of the nozzle bores (compare with the original five-hole nozzle tip in Fig. 1). Fig. 3 shows geometry projections of the three different nozzle types adapted for the TNH: isometric, side, and top views. The fuel flow enters the nozzle main bore from the top, and the pressure sensor is mounted at the bottom side in the isometric projection (see Fig. 2 for reference). The nozzle N101 represents the most straightforward arrangement of the three designs, where the nozzle bore is located centrally with reference to the main bore and perpendicular to the main bore axis. The nozzle N105 also has a centrally arranged nozzle bore but with an angle of 75°. The nozzle N104 has a perpendicular angle as well, but the nozzle bore is 0.8 mm eccentrically arranged. The nozzle bore and main bore diameters are identical for all three nozzles and are 0.75 mm and 3.5 mm, respectively.

2.3. Optical imaging

The TNH is designed to visualize the in-nozzle flow using a line-of-sight optical measurement technique like Shadowgraph imaging, where a light source illuminates one side of the transparent nozzle and an imaging system is installed on the other side. A schematic of the optical setup used is depicted in Fig. 4 where a simplified drawing of the fuel injector (j) together with the mounted TNH (d) is depicted as well, indicating the proportions. The dashed line indicates the optical axis. The setup used consisted of a Cavitar Cavilux Smart diode laser (i) emitting at a center wavelength of 640 nm together with a Questar QM100 far-field microscope (b) and a Photron Fastcam SA5 CMOS high-speed camera (a). A diffuser plate (e) has been installed in front of the TNH to guarantee a uniform background illumination. An

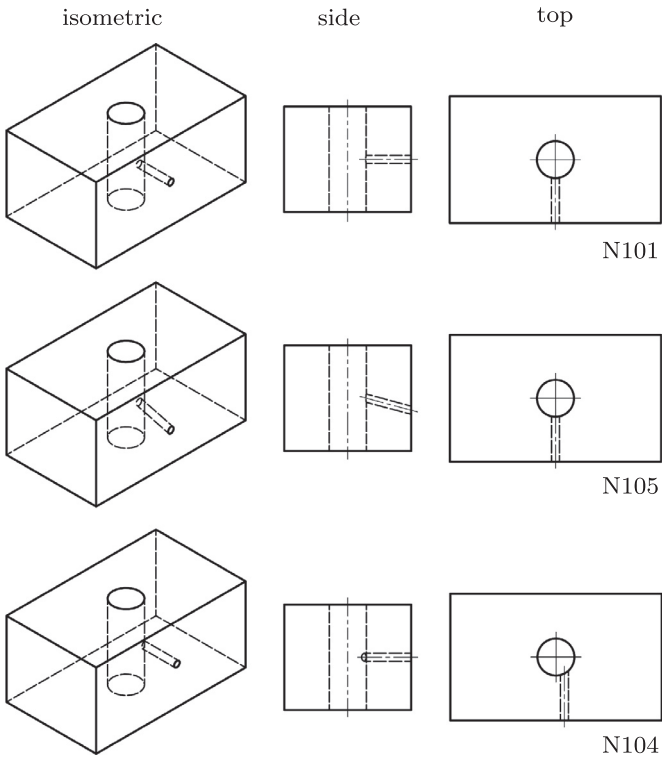

Fig. 3. Isometric, side, and top projection of the three different transparent nozzle types used. N101: centrically arranged 90° setup, N105: centrically arranged 75° setup, and N104: eccentrically arranged 90° setup. The main bore diameter is 3.5 mm and the nozzle bore diameter is 0.75 mm.

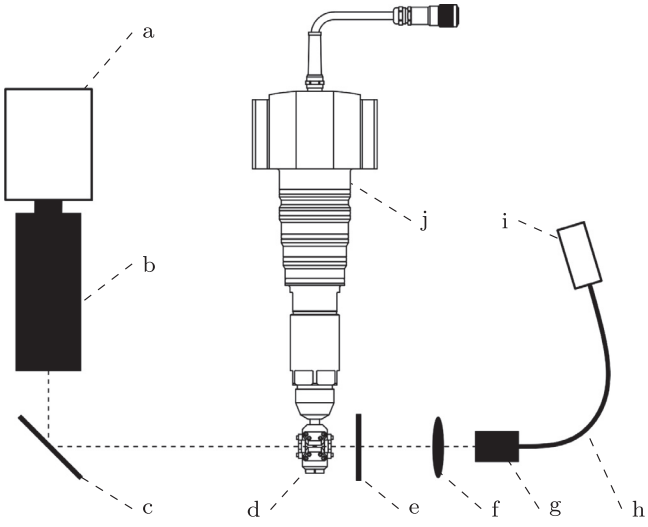

Fig. 4. Schematic of the optical setup used with high-speed camera (a), far-field microscope (b), mirror (c), transparent nozzle holder (TNH) (d), diffuser plate (e), focusing lens (f), collimator (g), optical light guide (h), diode laser (i) and injector (j). The dashed line represents the optical axis. Note that the spray chamber surrounding the TNH is not illustrated.

additional 150 mm plano-convex spherical lens (f) has been used together with an optical light guide (h) and its matching collimator (g) to focus and concentrate the diode laser emission onto the diffuser plate in front of the TNH (d). A mirror (c) has been used to protect the far-field microscope from possible debris in case of material failure. The field of view of approximately 5 x 5 mm has been acquired with a resolution of 512 x 512 pixels and a framerate of 20 kHz.

The use of a pulsed light source with short pulse lengths is necessary to acquire sharp in-nozzle flow images under realistic fuel pressure conditions. This is due to motion blur that would occur with a constant light source because of the relatively long exposure times in the range of µs compared to the fuel velocities of a couple 100 m/s in the nozzle bore.

2.4. Impingement measurements

To quantitatively characterize the different single-hole nozzle geometries, the spray momentum flux has been measured using a calibrated piezoelectric force sensor (type 9215a) together with a charge amplifier (type 5064) from Kistler. The so-called impingement measurements are further described in [25,26] and use conservation of momentum based on the assumption that the spray impingement area is much smaller than that of the sensor used in the measurements. Hence, the momentum flux of the spray at the nozzle bore exit is identical to the force measured on the sensor.

To align the force sensor exactly on the nozzle bore symmetry axis, three different sensor holders have been manufactured according to the different nozzle geometries. The force sensor holders have been mounted directly on the two top clamps of the TNH (see Fig. 2 for further details) to minimize the distance between the nozzle bore exit and the force sensor.

The momentum flux $\dot{M}_f$ can be calculated using Eq. 2:

$$\dot{M}_f = \int_{A_0} v^2 \cdot \rho \cdot dA \tag{2}$$

where A_0 is the geometrical area of the nozzle bore exit, and ρ and v the density and velocity of the fluid in liquid or gaseous phase exiting the nozzle bore.

2.5. Test facility

The experiments have been conducted in the constant-volume Spray and Combustion Chamber (SCC) at WinGD, where the geometry represents the combustion volume with the piston at top dead center of an RT-flex50 engine from WinGD's portfolio. The SCC is able to operate under realistic engine loads regarding charge pressures, swirl motion, and temperatures. The chamber diameter is identical to the cylinder bore and measures approximately 500 mm (more details about the test rig can be found in [2–4,6,27,28]). The fuel is pressurized using a standard common-rail system equipped with an injection control unit (ICU) as used on each cylinder of the RT-flex engines. The rail pressure has been set to 50 MPa, which represents a standard value at part load engine operation. Since only the in-nozzle flow has been investigated for this work, the back-pressure and gas temperature in the spray chamber have been set to ambient conditions. Experiments have shown that the back-pressure and fuel temperature play a less significant role for the in-nozzle flow cavitation patterns when the pressure differences are large and the fuel temperatures less than 80°C [29–31]. The fuel used is a standard Diesel from Preem AB with the product code DMK1UA-SE, a density of 815.9 kg/m^3 (at 15°C), a viscosity of 2.112 mm^2/s (at 40°C) and a net heat of combustion of 43.16 MJ/kg.

3. Numerical modeling

3.1. In-nozzle flow CFD simulations

Modeling turbulent cavitating flows is a challenging task because of the complexity of the phenomenon itself and the highly dynamic interaction between phases and non-equilibrium thermodynamic states. Recent numerical simulations have proven the applicability of CFD in cavitating flow predictions, thus supporting experimental measurements and product development [32–35]. Most of the published numerical work is limited to small- and medium-sized engine fuel injectors and due to large geometrical differences, only insufficiently useful for the validation and optimization of cavitation formation in large marine Diesel engine fuel injectors.

Several different models have been developed for cavitation in nozzles. Giussani *et al.* [36] provide an extensive overview of numerical modeling approaches of cavitating flows in fuel injector nozzles. The available methodologies for simulating multiphase flows can be classified either according to the adaptation of the multiphase fluid modeling or according to the mass transfer mechanism assumed for cavitation. Concerning multiphase modeling in Diesel fuel nozzles involving cavitation, the most common implementations are the homogeneous mixture models, the heterogeneous multi-fluid models, and the Lagrangian models.

The homogeneous Eulerian flow model has been utilized in [37,38] with a separate transport equation for the vapor volume fraction describing the evolution of the cavitation region. It is assumed that all the phases share the same velocity and pressure;;; the fluid is a continuous mixture of liquid and vapor. Most models rely on the assumption of thermodynamic equilibrium. The occurrence of cavitation is determined based on a cavitation criterion, in the simplest case, just by means of the local pressure in comparison with the vapor pressure. Dabiri *et al.* [39] tested this simple criterion and found that the viscous stress contributes to the size of cavitating regions significantly and thus leads to earlier cavitation inception [40].

Multi-fluid Eulerian models [41,42] allow a more detailed description of the flow compared to the homogeneous model. This method is characterized by different sets of conservation equations, one for each phase; thus each phase has its own velocity, temperature, and pressure [43]. However, the two-fluid model is based on time and space averaged equations and cannot track the interface explicitly.

When the cavitation level is low and the resulting bubbles are smaller than the cells in the computational grid, it is possible to use the Euler-Lagrangian approach. In this approach, each bubble as product of cavitation is tracked in a Lagrangian frame. Here, only the liquid is a continuum, while the vapor is the dispersed phase and is represented by parcels of bubbles. Vapor bubble trajectories are tracked, integrating the Newton equation of motion for each parcel. Examples of this method applied to nozzle flows are reported by Giannadakis *et al.* [44,45].

The widely-applied sharp interface capturing method Volume of Fluid (VOF) technique [36,43,46,47] has been chosen to capture the liquid/gas interface. The model is similar to the homogeneous model, where a single momentum equation is calculated for all phases that interact using the VOF model. The method is suitable to capture small to large scale deformations and interface zones as it is an Eulerian-Eulerian method, and therefore, the liquid and vapor are treated in separate phases. The cavity shape is constantly tracked and updated until the local pressure inside the cavity reaches the vapor pressure, therefore giving precise and convergent modeling of the cavity-surrounding liquid interface. The VOF method is able to successfully predict the separation point, recirculation zone, and reattachment points. Furthermore, the pressure distribution inside the compressible flow is also correctly captured. The solved transport equation of the vapor fraction predicts the convection of bubble nuclei or micro-bubbles within the liquid caused by cavitation. The basic drawback of this approach is the high numerical grid resolution required to sufficiently resolve the length and time scales. In this particular study, the VOF method has been chosen to track the interface of different phases. High Resolution Interface Capturing (HRIC) [48,49] has been applied in the VOF method to avoid artificial effects and to minimize numerical diffusion and compressive character. VOF and HRIC governing equations can be found in [49,50].

3.2. Cavitation model

The numerical representation of cavitation and flash boiling has been an important area of research due to the difficulties of representing their physics by robust and accurate numerical methodologies. Schmidt *et al.* [37] and Giannadakis [44] provide an extensive discussion on various models available. A widely-used Eulerian approach to simulate cavitation is based on the Rayleigh-Plesset equation, which describes the growth and collapse of a bubble in a liquid, assuming no slip between the two phases. This model is highly dependent on the initial bubble radius and number parameters, which can be defined by using prior experimental data data. In [51], Neroorkar *et al.* simulated cavitation phenomenon based on the Homogeneous Relaxation Model (HRM), thus providing an alternative to the Rayleigh-Plesset equation. In his study, it has been found that despite the differences between cavitation (driven by pressure) and flash boiling (driven by temperature as well), these models are sufficiently similar to suggest that the HRM can also model cavitation [52,53]. The results have been validated against geometries experimentally evaluated in [51] and demonstrated that the model could could correctly reproduce the cavitation in a nozzle. Battistoni *et al.* [54], in their study, compared a mixture model in conjunction with the HRM phase change model with a multi-fluid model utilizing the Rayleigh bubble dynamics for phase change, and validated against experimental data. It has been concluded that from an engineering point of view, the two models showed good predictive capabilities.

The cavitation model implemented in the commercial software Converge has been used for this study. The model is based on the flash-boiling hypothesis of Shields *et al.* from 2011 [37,38,55,56] with rapid heat transfer between vapor and liquid phase. The method represents a similar procedure to cavitation, where the vapor formation happens through a pressure drop on a constant temperature level, except that the pressure drop is lower and there is a temperature elevation in the system. The mass exchange between phases is predicted by an HRM, which describes the process of vapor mass fraction approaching its equilibrium state. This mass fraction rate is calculated by the formula:

$$\frac{D_x}{D_t} = \frac{\bar{x} - x}{\Theta} \tag{3}$$

where $\bar{x}$ represents the equilibrium mass of vapor phase, x is the instantaneous mass, and Θ is the time scale over which x relaxes to $\bar{x}$. For evaporation, Θ_E is expressed in Eq. 4, furthermore the condensation time scale is described by equation Eq. 5:

$$\Theta_E = \Theta_0 \cdot \alpha^{-0.54} \cdot \varphi^{-1.76} \tag{4}$$

$$\Theta_C = F \cdot \Theta_0 \cdot \alpha^{-0.54} \cdot \varphi^{-1.76} \tag{5}$$

where F is the condensation time scale factor with a typical value of 5E3, meaning that the condensation is 5E3 times faster than the evaporation under similar conditions. The Θ_0 coefficient is set to 3.84E-7 s based on validated work from [52,57,58]. The non-dimensional pressure ratio φ, is given by the formula:

$$\varphi = \frac{p_{sat} - p}{p_c - p_{sat}} \tag{6}$$

where p_c means the critical pressure. Further information of the cavitation model can be found in [50].

In the flow field, O_2 and N_2 representing the air inside the nozzle and the gas state of n-Dodecane as fuel surrogate have been initialized. The equation of state has been handled by the Redlich-Kwong cubic equation (shown in Eq. 7), while the real gas properties are calculated as a function of temperature.

$$p = \frac{RT}{v - b} - \frac{a}{v^2 + ubv + wb^2} \tag{7}$$

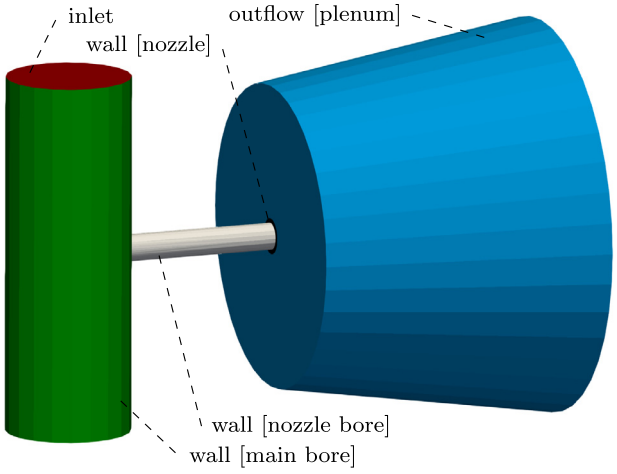

Fig. 5. Schematic Figure of CFD domain with applied boundary conditions presented for nozzle type N101.

Further information of the coefficients can be found in [50].

Based on its very similar physical properties compared to the measured Diesel fuel, n-Dodecane has been utilized as Diesel surrogate.

3.3. Turbulence modeling

RANS and URANS simulations have been popular within the industry due to time and cost constraints, predicting flows acceptably on a macroscopic level. LES, DES, and hybrid RANS/LES approaches, among other turbulence models, still have high computational demand but resolve transient large-scale turbulent structures and provide more detail of the flow [59,60]. Koukouvinis *et al.* [61], in their extensive work, tested several turbulence models with different cavitation models at many pressure drops and compared those results to experimental data. They found that RANS produced less accurate results at low-pressure drops. Edelbauer *et al.* [62] compared RANS and LES of cavitating flows and concluded that RANS could predict cavitation with reasonably acceptable accuracy in an operating condition with high-pressure difference. In the present high-pressure injection study, the Renormalization Group (RNG) $k-\epsilon$ turbulence model has been applied. The model coefficients have been taken from the literature and follow the instructions for cavitating flows in Diesel injectors suggested by Convergent Science. Further information on the turbulence kinetic energy and turbulence dissipation equations can be found in [50].

3.4. Numerical setup

The CFD domain with the applied boundary conditions can be seen in Fig. 5. The nozzle is modeled as wall boundary. Static pressure derived from the measurements is applied at a fuel temperature of 323 K at the nozzle inlet. The mass fraction of the entering fuel is 99.9% of n-Dodecane and 0.1% of air. The turbulent intensity and length scale are approximated and set to 0.02, and 0.0001 m, respectively. The nozzle walls are treated as no-slip walls assuming smooth wall conditions. The plenum, which is a constant volume filled with air, has atmospheric conditions. Here, the outflow boundary condition is applied. The turbulent kinetic energy is specified at a value of 0.02 and the length scale is set to have a value of 0.0003 m. Together with the wall boundary conditions, the law of the wall for high-Reynolds number applications is applied. In the absence of prism layers, the viscous sub-layer of the bound-

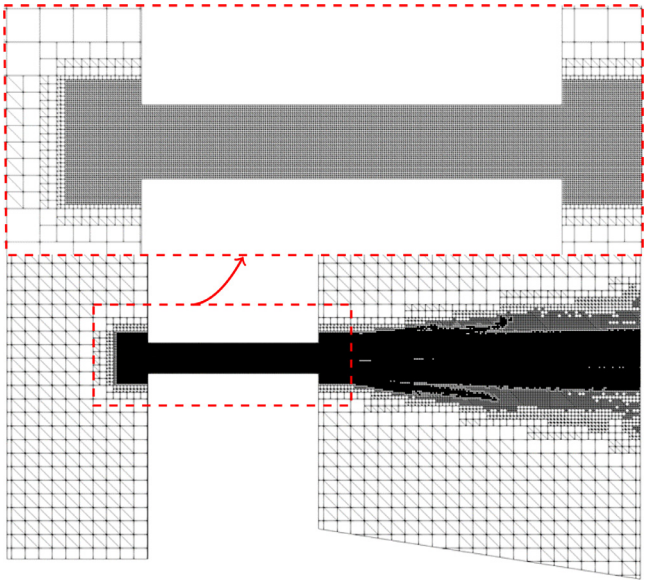

Fig. 6. Grid structure applied in the simulation in case of the nozzle type N101 with a detailed view around the nozzle bore (top).

ary layer cannot be sufficiently resolved; therefore the application of the wall function is obligatory. The law of the wall approach is a logarithmic curve fit of the turbulent boundary layer; thus the tangential components of the stress tensor can be calculated. The simulation is set to reach a quasi-steady solution at 0.01 s.

3.5. Grid generation

Three different grids have been created for the standard nozzle N101 in order to investigate the grid resolution influence on the computational results. Based on the nozzle bore diameter of 0.75 mm, 40, 35, and 30 cells have been placed in the nozzle bore, respectively. With the aforementioned nozzle bore resolution, a base grid size has been calculated for the entire geometry of the nozzle.

The nozzle bore region has been computed by the so-called fixed embedding, utilizing a scaling factor of 4 compared to the chosen base cell size, where a stationary zone has been defined including the nozzle bore length, the vicinity of the nozzle bore inlet and the near nozzle bore region inside the plenum (see Fig. 6). The plenum region has been computed by Adaptive Mesh Refinement (AMR), where the automated grid refinement cuts the cells by a scaling factor of four, based on velocity and void fraction sub-grid criteria. The wall boundaries have been computed by a permanent grid resolution by keeping the non-dimensional wall distance value y^+ at 30, which is appropriate in case of high-Reynolds number turbulent flow applications.

3.6. Solver settings

The transient solver with the full hydrodynamic simulation mode has been chosen for this application. Both the gas and liquid flow solvers are fully compressible. The Pressure-Implicit with Splitting of Operators (PISO) algorithm with a tolerance of 0.001 has been used for the pressure-velocity field coupling, while the momentum, pressure, density, and energy equations have been taken care of the linear solver method, thus allowing a faster convergence. The time step has been set to be varied between 1E-10 and 1E-06 s, while the maximum CFL (Courant-Friedrichs-Lewy condition) number and diffusive CFL number have been chosen to be lower than 0.25 and 0.5, respectively.

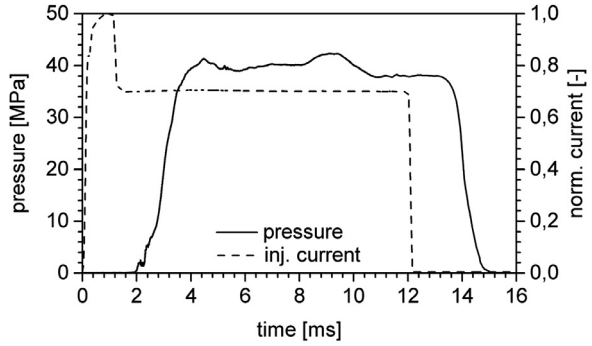

Fig. 7. Averaged fuel pressure and injector solenoid current for injection duration of 12 ms. The time origin is triggered start of injection (tSOI).

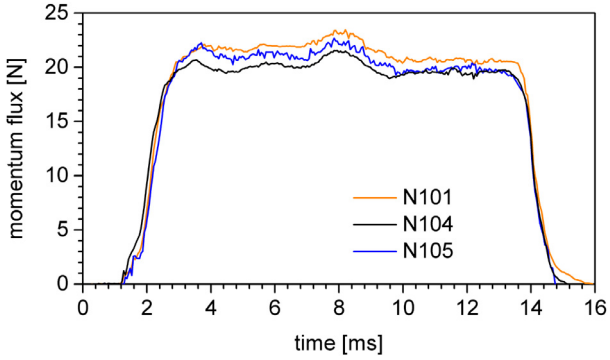

Fig. 8. Averaged momentum flux $\dot{M}_f$ of the three different nozzles used over the injection duration. The time origin is triggered start of injection (tSOI).

4. Results and discussion

4.1. Experimental results

The fuel pressure measured in the main bore of the nozzle mounted in the TNH and the corresponding normalized current signal of the injector solenoid are depicted in Fig. 7. The signals shown are averaged over 20 injections. The time axis origin is the triggered start of injection (tSOI). The shift between current and pressure signal indicates the hydraulic delay due to the needle movement in the fuel injector. The quasi-steady-state injection period has been defined between 5 and 13 ms after tSOI and has been used to average the pressure, the momentum flux, and the in-nozzle flow images for comparison with the CFD results. The depicted pressure curve in Fig. 7 represents the data of the nozzle type N101. As there is no significant difference in the pressure signals of the three nozzle types, the pressure curves of the nozzles N104 and N105 are not depicted for visibility reasons.

The momentum flux data acquired for the three different nozzles used is depicted in Fig. 8. Note the similar curve characteristics compared with the pressure curve shown in Fig. 7. The pressure and momentum flux results have been averaged over the quasi-steady-state period of the fuel injection process between 5 and 13 ms after tSOI. The averaged values and the corresponding standard deviations of the pressure measurements are depicted together with the momentum flux results from the impingement measurements in Table 1. The averaged pressure data has been used for the CFD boundary conditions.

Although the quasi-steady-state period of the pressure and momentum flux curves show fluctuations, the signal is very stable, as indicated by the small standard deviations as sown in Table 1 - tt hose fluctuations originate from the hydraulic high-pressure system providing the injector with fuel and are fully reproducible.

Table 1
Experimentally measured and averaged fuel pressure and momentum flux $\dot{M}_f$ together with the standard deviation for the three different nozzle types (N101, N104 and N105) investigated.

		measurements
avg. pressure N101	[MPa]	38.51 ± 1.08
avg. pressure N104	[MPa]	38.98 ± 1.04
avg. pressure N105	[MPa]	38.32 ± 1.00
avg. $\dot{M}_f$ N101	[N]	21.46 ± 0.09
avg. $\dot{M}_f$ N104	[N]	19.97 ± 0.07
avg. $\dot{M}_f$ N105	[N]	20.93 ± 0.11

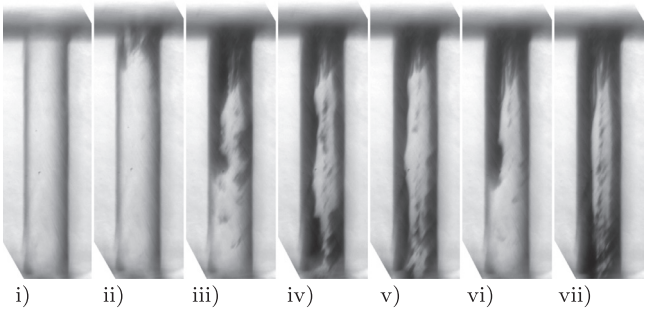

Fig. 9. In-nozzle images of nozzle N101. Note that dark areas within the nozzle bore indicate gaseous flow, i.e., cavitation. Nozzle bore filled with Diesel, but no cavitation flow (i), first sign of cavitation (ii), and following image frames with 50 μs time interval (iii - vi), and during quasi-steady-state fuel injection at around 8 ms after tSOI (vii).

The acquired images of the in-nozzle flow have only been intensity adjusted, rotated and cut, to remain the maximal image information. A series of selected in-nozzle flow images are shown in Fig. 9 where i) shows the with Diesel fuel filled nozzle bore before the needle opening, ii) - vi) during needle opening, and vii) during the quasi-steady-state fuel injection at around 8 ms after tSOI. The field of view used covers the entire nozzle bore (vertical) of the transparent nozzles and a small area of the nozzle main bore (horizontal, top of image). Since the refractive index of the PMMA material and the Diesel fuel used are not perfectly identical, the main bore and nozzle bore walls are visible at all times in the images acquired. Therefore, the image before needle opening, as depicted in Fig. 9 i), serves as a reference background. In the other images shown in Fig. 9, the additional dark areas represent gaseous flow, i.e., cavitation. The light is refracted away from the optical axis due to the phase and consequent refractive index change and therefore does not arrive on the camera sensor. The bright areas within the walls of the nozzle bore indicate the liquid fuel flow as the light passes the transparent nozzle with only slight distortions and arrives on the camera sensor. For comparison with the CFD results, only the images during the quasi-steady-state injection period as depicted in Fig. 9 vii) have been used and averaged. However, the images acquired during needle opening (Fig. 9 ii) - vi)) are quite interesting as well. Image ii) represents the in-nozzle flow at around 2.1 ms after tSOI (compare with the pressure curve in Fig. 7) and shows the first cavitation in the acquired measurement series. The pressure is still quite low compared to the maximal pressure achieved roughly 1 ms later. The following images iii) to vi) are the consecutive frames with 50 μs interval given by the 20 kHz frame rate of the high-speed camera. The cavitation development within these five sequential images is interesting since the cavitation pattern develops to supercavitation in image vi) and then forms back to film and cloud cavitation as shown in images iii) and vi) [16,63]. This reduction in cavitation intensity can be traced back to the small pressure fluctuation at the beginning of the pressure curve, as depicted in Fig. 7. Another interesting fact is the very similar supercavitating pattern in image v) and vii) although the pressure difference with approximately 40 MPa is extensive (compare with pressure curve in Fig. 7, image v) acquired at around 2.25 ms and image vii) at around 8 ms after tSOI).

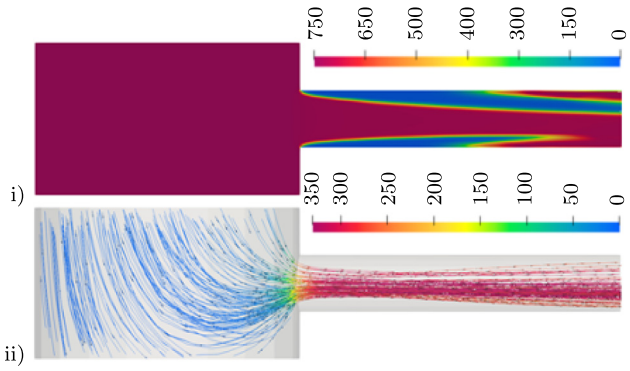

Fig. 10. Density distribution [kg/m^3] shown in a vertical section cut in the middle of the nozzle bore (side view) for the nozzle type N101 (i), while streamlines colored by velocity magnitude [m/s] give the flow path inside the nozzle (ii) taken at the end of the simulation.

4.2. CFD in-nozzle flow investigation

A grid sensitivity analysis investigating three different numerical grids has been executed by utilizing the standard nozzle N101. After reaching a converged quasi-steady solution, the spray Reynolds number of each mesh type, based on the velocity magnitude values stored in a section 0.05 mm before the nozzle bore, has been defined. Here, the flow field has been sampled along a straight line in the nozzle bore cross-section in 50 points. Then, the grid types have been compared by means of averaged pressure, density, and velocity fields, as well as by taking the cell gas fractions at the nozzle bore exit. It can be stated that only minor deviations among the test grids could be found. The finest grid predicts the highest maximum velocity magnitude at the nozzle bore exit, while the coarsest grid shows a loss in velocity magnitude by approximately 20 m/s. The average velocity magnitude analyzed at the same cross-section of the nozzle bore results in very similar behaviour. Furthermore, the test meshes have been compared by means of time-averaged Mach number and cell densities stored in the sampling points. The coarser grid resulted in very similar values in any investigated physical flow properties to the finest grid and still having remarkably less computational time. As a result, the grid spacing of the coarser grid has been utilized for all three nozzle layouts for further numerical investigations.

Each of the three nozzles has been analyzed individually. A vertical cross-section cutting the nozzle bore exactly in the middle and visualizing the density distribution inside the nozzle is depicted in Fig. 10 i). Note that only the side view of the nozzle geometry is visualized for visibility reasons. The density distribution shows not just a separation of flow at the sharp nozzle bore inlet but also a flow detachment close to the nozzle bore exit can be seen, which has a pronounced effect on the spray formation. Regarding the pressure field (not presented here), one can state that the pressure reduces while entering the nozzle bore, where the fuel velocity increases according to Bernoulli's law. The local pressure at the nozzle bore inlet drops below the vapor pressure of the fuel at the given temperature level, and additionally, the sudden geometrical change invokes immediate cavitation inception.

Streamlines colored by velocity magnitude (see Fig. 10 ii)) show the path of the fuel inside the nozzle, with a vena contracta represented by the compressed streamlines after the fuel enters the

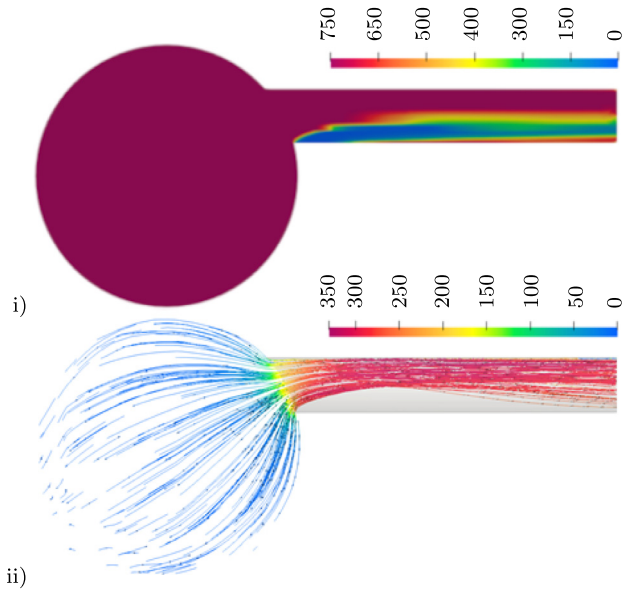

Fig. 11. Density distribution [kg/m^3] shown in a vertical section cut in the middle of the nozzle bore (top view) for the nozzle type N104 (i), while streamlines colored by velocity magnitude [m/s] give the flow path inside the nozzle (ii) taken at the end of the simulation.

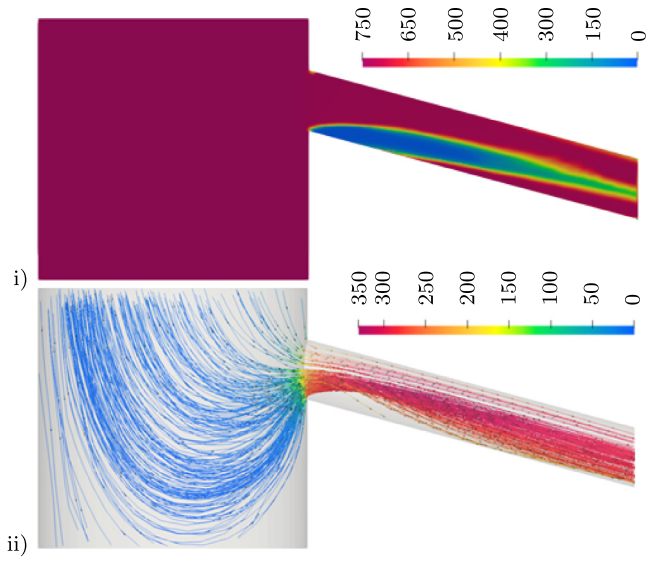

Fig. 12. Density distribution [kg/m^3] shown in a vertical section cut in the middle of the nozzle bore (side view) for the nozzle type N105 (i), while streamlines colored by velocity magnitude [m/s] give the flow path inside the nozzle (ii) taken at the end of the simulation.

nozzle bore from the main bore. A more pronounced separation can be seen on the upper side of the nozzle bore, which is expected since the fuel enters directly from the nozzle main bore inlet direction and therefore suffering a significant redirection caused by the geometrical properties of the nozzle.

The cavitating flow simulation results from the eccentric nozzle N104 are depicted in Fig. 11. Note that only the top view of the nozzle geometry is shown for visibility reasons. The flow field is described in terms of density distribution (i) and velocity field (ii) inside the nozzle. The flow enters the nozzle bore through a significant distortion caused by the sharp inlet formed by the eccentrical arrangement. Flow separation inside the nozzle bore on the nozzle main bore symmetry side occurs, and as a result, a large recirculation zone is created, which is filled by fuel vapor. The region extends until the nozzle bore exit, forming a massive vapor tube inside the nozzle bore and therefore significantly reducing the effective area of the nozzle bore. The eccentric side of the nozzle bore seems to be undisturbed by the geometry and as a result, the presence of a remarkably high-velocity zone can be found. The highly non-uniform velocity magnitude distribution is an obvious outcome of the nozzle bore eccentricity and the geometrically induced cavitation. The cavitation zone at the nozzle bore inlet detaches after approximately a distance of one nozzle bore diameter and separates from the nozzle bore wall into the internal region of the nozzle bore. The extended and coherent vapor zone reaches the nozzle bore exit while vapor bubbles travel through the flow. This sort of vapor formation is a typical characteristic of string cavitation and supercavitating nozzles [18,64]. Vapor formation can also be seen at the nozzle bore exit, which significantly influences the spray formation and causes spray core deformation.

The CFD results of the angled nozzle N105 are depicted in Fig. 12. Note that only the side view of the nozzle geometry is presented for visibility reasons. The density distribution (Fig. 12 i) shows an extended separation zone on the bottom side of the nozzle bore initiated by the sudden geometrical change at the nozzle bore inlet. This zone evolves into the fluid domain, compressing the velocity streamlines (Fig. 12 ii) to the upper side of the nozzle bore, creating an area with high velocities. The upper edge of the nozzle bore inlet shows a comparably very small depression zone, which can be identified as cavitation inception at the nozzle bore inlet; however it does not seem to have a significant effect on the flow field.

Table 2
Summary of the flow properties of the three nozzle types based on the CFD simulation results.

		nozzle types		
		N101	N104	N105
avg. v_{mag} at orifice	[m/s]	296	278	285
avg. Re at orifice	[-]	69.9k	65.6k	67.2k
velocity uniformity index U_i	[%]	94	89	96
avg. cell gas fraction at orifice	[%]	31	30	23
discharge coefficient C_D	[-]	0.65	0.62	0.69
momentum flux $\dot{M}_f$	[N]	21.06	18.81	21.71

A summary of the nozzle and flow field properties of the CFD simulation results can be found in Table 2.

Taking the average velocity magnitude evaluated by the CFD simulations at the nozzle bore exit (orifice), the standard nozzle N101 has the highest velocity and the eccentric nozzle N104 the lowest. Based on these velocities, the corresponding Reynolds numbers (Re) have been defined for all three nozzle geometries, proving the presence of highly turbulent flow. The velocity magnitude distribution in the vicinity of the nozzle bore exit can be defined by the velocity uniformity index U_i introduced by Weltens *et al.* [65] described in Eq. 8,

$$U_i = \left[1 - \frac{1}{2n}\sum_{i=1}^{n}\frac{\sqrt{(v_z - \overline{v_z})^2}}{\overline{v_z}}\right] \cdot 100 \tag{8}$$

where n is the total number of cells considered, v_i is the axial velocity in the cell and $\overline{v_z}$ represents the mean axial velocity. The velocity uniformity index U_i shows uniform flow velocity distribution arriving at the nozzle bore exit for the standard and the inclined nozzles (N101 and N105, respectively) while the eccentric nozzle N104 stays by a few percentage points behind (see Table 2 for further details). Another indicator of the flow uniformity is the void fraction of phases at the nozzle bore exit. Therefore, averaging of the gas fraction of cells has been executed using the CFD simulation results. The standard N101 and the eccentric nozzle N104 have

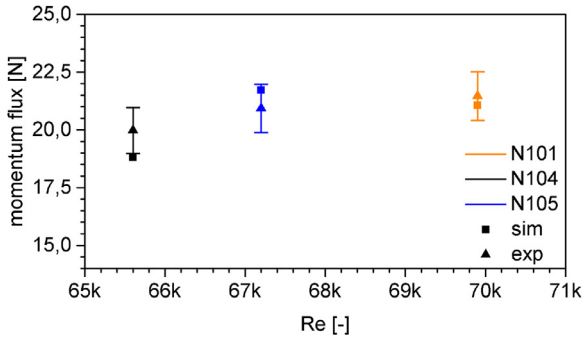

Fig. 13. Experimental and simulated momentum flux ($\dot{M}_f$) of analyzed atomizer geometries as function of Reynolds number.

higher gas fraction, while the angled nozzle N105 results in less gas-phase content just right before entering the plenum. The discharge coefficient C_D gives a good indication of nozzle efficiency, wherewith the reduced effective nozzle bore area due to cavitation, the value decreases and therefore influences the injected fuel velocity. The eccentric nozzle N104 provides the lowest discharge coefficient, while the rest of the nozzles have slightly higher values (see Table 2 for reference). The momentum flux $\dot{M}_f$ has also been evaluated from the CFD simulation results as it remains the only quantitative result to compare directly with the experimental results. The angled nozzle N105 has the highest momentum flux and the eccentric nozzle N104 with a significant deviation, the lowest.

4.3. Comparison of experimental and numerical results

Fig. 13 depicts the momentum flux $\dot{M}_f$ from the experiments and simulations together with their Reynolds numbers (Re) evaluated from the CFD simulation results. The experimentally acquired momentum flux of the three different nozzle types shows error bars with a span of 5% to illustrate the deviations between experiment and simulation. Although the standard deviation of the measured and averaged force signals from the impingement experiments were evaluated (see Table 1), the errors are likely to be larger due to observational errors, and hence, a fixed span of 5% was chosen instead of the standard deviation of approximately only 0.1 N. The simulation results fit the experimental data well for nozzle type N101 while predicting a slightly lower value for the eccentric nozzle N104 and a slightly higher value for the angled nozzle N105. The standard nozzle N101 has the smallest discrepancy with less than -2% compared to the experimentally measured value.

Fig. 14, 15, and 16 show the experimentally acquired in-nozzle flow images compared to the CFD simulation results. To create CFD images that are qualitatively comparable to the experimental images, a time frame has been defined for statistical examination after the simulation has reached a quasi-steady-state. This allows a comparison to the outcome of the time-averaged experimental images. The Strouhal number, as non-dimensional shedding frequency of the emerging spray, has been determined by utilizing the occurred velocity at the nozzle bore exit. As a next step, a simulation time of six shedding periods has been chosen as time interval for a statistical examination of the simulation results.

The images in Fig. 14, 15, and 16 depict the acquired in-nozzle flow of the nozzles N101, N104, and N105, respectively. Similar to the experimental data presented in chapter 4.1, Fig. 9, the first image shows the background (i), which is the transparent nozzle filled with Diesel fuel but without fuel mass flow. The second image (ii) shows a single acquisition of the in-nozzle flow during the quasi-steady-state fuel injection at approximately 8 ms after tSOI. And the last image (iii) is correspondent to an arithmetic mean,

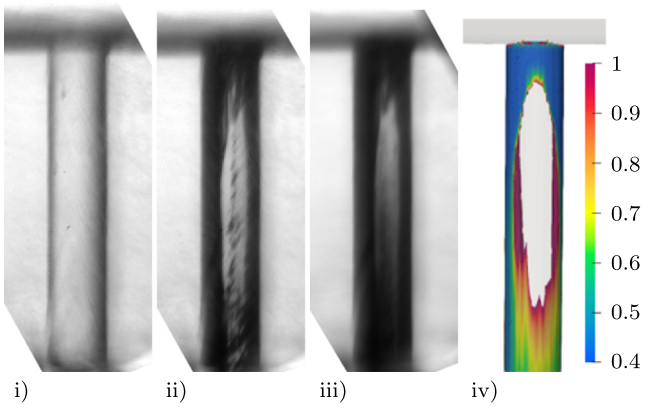

Fig. 14. Experimental in-nozzle flow images showing background (i), single-shot (ii), and average during injection (iii) together with the corresponding CFD result (iv) depicting isovolumes of cell fuel vapor pressure fraction in a non-dimensional range for the nozzle N101.

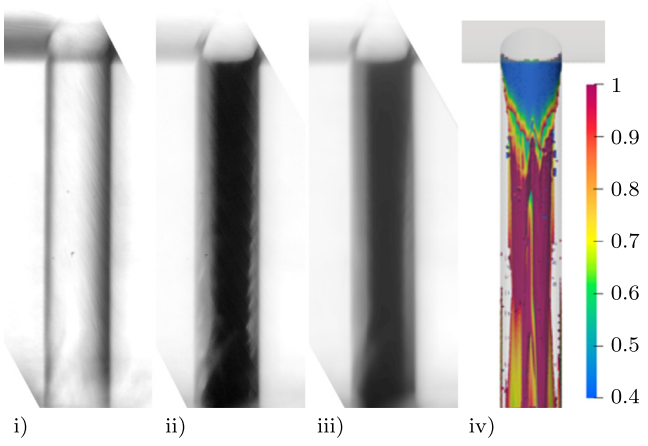

Fig. 15. Experimental in-nozzle flow images showing background (i), single-shot (ii), and average during injection (iii) together with the corresponding CFD result (iv) depicting isovolumes of cell fuel vapor pressure fraction in a non-dimensional range for the nozzle N104.

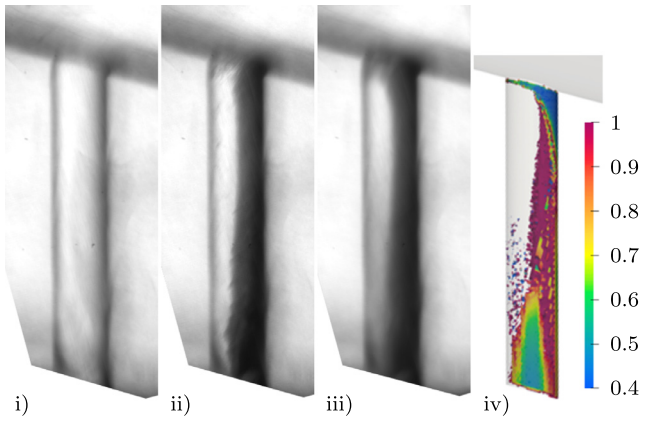

Fig. 16. Experimental in-nozzle flow images showing background (i), single-shot (ii), and average during injection (iii) together with the corresponding CFD result (iv) depicting isovolumes of cell fuel vapor pressure fraction in a non-dimensional range for the nozzle N105.

created by averaging the single frames over the quasi-steady-state injection period between 5 and 13 ms, which at the frame rate of 20 kHz are approximately 160 images per injection.

As the flow in the nozzle bore is cavitating, the light from the laser pulse is scattered away from the line-of-sight optical axis, and therefore the areas appear dark on the image. The Diesel fuel flow in the main bore is not cavitating, and hence, no dark areas appear in the visible areas. Some small optical distortions occur due to not perfectly polished surfaces on the PMMA nozzles, the transition between the PMMA nozzles and the sapphire bricks (see Fig. 2 for reference) and fuel deposits.

The standard nozzle design N101 with the centrically, 90° arranged nozzle bore (Fig. 14) is supercavitating as the gaseous phase reaches the nozzle bore exit [63]. The fuel flow enters the main bore from the left side and hence the cavitation in the nozzle bore on the left side is more distinctive. At the nozzle bore inlet, the flow is fully cavitating around the circumference; however, after approximately one times the diameter of the nozzle bore, the cavitation is limited to the two side walls. This film-like cavitation along the nozzle bore walls has been observed by Reid *et al.* [66] in their optical in-nozzle flow investigation as well. The single-shot image (ii) reveals the presence of transient cavitation in the middle of the nozzle bore; this cavitation bubble cloud travels close to the nozzle bore axis of symmetry towards the orifice, causing a darkening of the averaged image (iii). Interestingly enough, at the time instance when the single shot has been taken, despite injecting with full pressure, the vapor bubbles do not elongate and form string-like cavitating structure reported in previous studies [67]. CFD predicts very similar phenomena as the measurement; chosen isovolumes of cell fuel vapor pressure fraction using a threshold of 0.4 to 1 visualize the vapor formation along the entire nozzle bore. The extent and location of cavitation inception at the nozzle bore inlet show very good agreement between experiment and simulation. The presence of a coherent film-like vapor layer on the upper and lower walls of the bore reach the nozzle bore exit and indicate a pattern of supercavitation. Again, simulation and experimental results are in good agreement (Fig. 14 iv)).

The eccentrically arranged nozzle N104 (Fig. 15), where the nozzle bore has an angle of 90° and an eccentricity of 0.8 mm with respect to the axis of the main bore (see Fig. 3 for reference), shows a different cavitation pattern: due to the axis of the eccentricity, the cavitation zones refract most of the incoming light away, resulting in almost completely dark nozzle bores. The single-shot (ii) scarcely reveals non-cavitating zones on the left and right side of the nozzle bore, indicating that the supercavitation zone is rotated into the optical axis. The fuel flow also enters the horizontal main bore from the left side, although the cavitation patterns at the nozzle bore inlet indicate strong flow lines from the right side. This is due to the flow pattern in the nozzle main bore that diverts the flow as visible in the streamline CFD result for nozzle N105 in Fig. 12 ii). The measured average momentum flux shows that the eccentric nozzle has less beneficial flow properties compared with the other nozzle layouts investigated. CFD attains good agreement with the experiments (see Fig. 15 iv)). As a result of the eccentric nozzle arrangement, geometric-induced cavitation develops along the entire nozzle bore, reaching the orifice. Cavitation inception at the inlet of the nozzle bore shows strong similarities to the experimental data data. A completely asymmetric vapor formation is well captured (Fig. 11, Fig. 15), while the location of the cavitating zones is also well matched with the optical measurement results. Approximately at 2/3 times of the nozzle bore length, both experiments and simulation reveal the reattachment of vapor layer onto the upper and lower walls of the bore. The presence of the intact vapor cloud experienced in the flow field results in the lowest discharge coefficient and velocity uniformity index among the nozzles investigated (Table 2).

In the case of the 75° angled, centrically arranged nozzle bore design N105 (Fig. 16), the images are rotated so that the nozzle bore walls appear vertical. As a result, the nozzle main bore on the upper side of the images is angled. The fuel enters the main bore from the left side. N105 nozzle also shows supercavitation. However, the cavitation zone is completely focused on the right side of the nozzle, where the angle between main and nozzle bore remains the sharpest. There are some additional small cavitation patterns at the nozzle bore inlet, but these, instead of elongating and forming strings (as observed in [68]), dissipate immediately, leaving all geometrical cavitation to one side of the nozzle bore. After approximately 1/3 times the bore length, the gaseous region expands and grows towards the orifice. N105 shows the most moderate level of cavitation compared to the other two nozzle designs. This also can be proven by examining the results of the numerical simulation (Fig. 16 iv)). CFD results clearly show the lowest average cell gas fraction at the orifice for N105. Furthermore, the highest velocity uniformity index and discharge coefficient have been obtained by simulating the N105 design (see Table 2). It must be noted that the small dark area on the left side at the nozzle bore exit is an optical distortion and not cavitating flow as clearly visible by comparing the background (i) with the single-shot (ii) and averaged (iii) images.

5. Conclusions

In this study, a TNH together with transparent PMMA nozzles have been successfully used to acquire reliable in-nozzle flow images under large two-stroke marine Diesel engine like fuel pressure conditions. Three simplified (one-hole instead of five-hole setup) real-size cylindrical nozzle geometries with real Diesel fuel have been tested. Interpretation of the acquired experimental images has been supported by CFD predictions of the in-nozzle flow. The experimental in-nozzle flow visualization has shown cavitation patterns in the nozzle bore with high contrast and temporal resolution. Impingement measurements have been executed to provide quantitative comparison of the nozzle performance and to validate CFD simulations. A ddiscrepancy of less than 6% between experiment and simulation has been achieved. Calculated nozzle discharge coefficients and cell vapor fractions analyzed at the orifice present very similar trend to those of experimental findings of this study. CFD results have accurately captured the location and extent of cavitation inception for all nozzle layouts investigated. In all cases, the predicted vapor formation inside the nozzle bore shows a good match compared with experiments. The quantitative and qualitative comparisons of the cavitation patterns have proven the applicability and functionality of the CFD simulation presented.

Significant differences among the nozzle layouts have been found. Clearly, the geometric characteristics of the nozzle bore location and its direction have a dominant effect on the type, volume and evolution of cavitation formation. Cavitation in the standard nozzle design (N101) is characterized mainly by cavitation inception at the bore inlet and film-like cavitation along the upper and lower walls of the nozzle bore reaching the orifice. Interestingly enough, the evolution of cavitation over time shows the development of supercavitation and, then at a later stage, by reaching a quasi-steady state, the reappearance of cloud and film-like cavitation formation. The eccentric nozzle bore arrangement (N104) is responsible for a highly asymmetric flow field and thus vapor formation in the nozzle bore. The injected fuel suffers significant losses after entering the nozzle bore. A large extent of separation zone forms on the opposite side of eccentricity. Supercavitation is present on the left side of the bore, initiated from the sharp inlet and reaching the bore exit. Regarding the angled nozzle (N105), supercavitation also can be realized. Vapor formation appears at the sharp inlet between main and nozzle bore and then develops along

the entire nozzle bore, mainly located on one side of the nozzle. Small bubbles dissipate at the nozzle bore inlet without evolving into more extended cavitation volumes. After approximately 1/3 times the nozzle bore length, the gaseous zone expands and grows towards the orifice. The comparison of the three nozzles suggests that the standard nozzle N101 has the highest velocity and most turbulent flow, while the eccentric nozzle (N104) gives the lowest values in this regard. Using the N104 eccentric nozzle geometry gives the lowest discharge coefficient, thus being the most disadvantages choice among the nozzles tested. The angled nozzle N105 produces by far the lowest level of cavitation, the highest discharge coefficient, and highest momentum flux. Therefore, the N105 design is the optimal nozzle layout to be used as atomizer for large two-stroke marine Diesel engine injectors. These findings will be further used as start of a more detailed investigation on large two-stroke marine Diesel engine injector nozzle optimization.

Declaration of Competing Interest

The authors declare that they have no known competing financial interests or personal relationships that could have appeared to influence the work reported in this paper.

CRediT authorship contribution statement

Reto Balz: Conceptualization, Investigation, Visualization, Writing - original draft. **Imre G. Nagy:** Conceptualization, Investigation, Visualization, Writing - original draft. **German Weisser:** Writing - review & editing. **David Sedarsky:** Supervision, Project administration, Funding acquisition.

Acknowledgments

The authors would like to thank the Combustion Engine Research Center (CERC) affiliated to Chalmers University of Technology, the Swedish Energy Agency and the Swiss Federal Office of Energy for financial support. Special thanks go to Lorenzo Testa (Convergent Science) for the provided support during the project.

References

[1] IMO, International Shipping Facts and Figures – Information Resources on Trade, Safety, Security, Environment, Technical Report, 2012.
[2] K. Herrmann, Development of a reference experiment for large diesel engine combustion system optimization, in: Proceedings of the Congress of the International Council on Combustion Engines (CIMAC),Vienna, Austria, 2007.
[3] A. Schmid, B. von Rotz, R. Schulz, K. Herrmann, G. Weisser, R. Bombach, Influence of nozzle hole eccentricity on spray morphology, in: ILASS-Europe, 25th European Conference on Liquid Atomization and Spray Systems,Chania, Greece, 2013.
[4] A. Schmid, C. Habchi, J. Bohbot, B. von Rotz, K. Herrmann, R. Bombach, G. Weisser, Influence of in-nozzle flow on spray morphology, in: ILASS-Europe, 26th European Conference on Liquid Atomization and Spray Systems, Bremen, Germany, 2014.
[5] I. Nagy, A. Schmid, S. Hensel, C. Dahnz, Computational analysis of spray primary breakup in 2-stroke marine diesel engines with different nozzle layouts, in: ICLASS 2015, 13th Triennial International Conference on Liquid Atomization and Spray Systems, Tainan, Taiwan, 2015.
[6] I. Nagy, A. Matrisciano, H. Lehtiniemi, F. Mauss, A. Schmid, Influence of Nozzle Eccentricity on Spray Structures in marine diesel sprays, SAE Technical Paper 2017-24-0031 (2017).
[7] A. Andriotis, M. Gavaises, C. Arcoumanis, Vortex flow and cavitation in diesel injector nozzles, J Fluid Mech 610 (2008).
[8] M. Blessing, G. König, C. Krüger, U. Michels, V. Schwarz, Analysis of Flow and Cavitation Phenomena in Diesel Injection Nozzles and its Effects on Spray and Mixture Formation, SAE Technical Paper 2003-01-0013 (2003).
[9] N. Mitroglou, M. Gavaises, J. Nouri, C. Arcoumanis, Cavitation inside enlarged and real-size fully transparent injector nozzles and its effect on the near nozzle spray formation, DIPSI Workshop 2011 on Droplet Impact Phenomena and Spray Investigation, Bergamo, Italy, 2011.
[10] R. Payri, J. Gimeno, G. Bracho, D. Vaquerizo, Study of liquid and vapor phase behavior on Diesel sprays for heavy duty engine nozzles, Appl Therm Eng 107 (2016).
[11] Z. Falgout, M. Linne, Novel design for transparent high-pressure fuel injector nozzles, Rev. Sci. Instrum. 87 (2016).
[12] S. Yang, X. Li, D. Hung, M. Xu, Characteristics and correlation of nozzle internal flow and jet breakup under flash boiling conditions, Int J Heat Mass Transf 127 (2018).
[13] B. Kim, S. Park, Study on in-nozzle flow and spray behavior characteristics under various needle positions and length-to-width ratios of nozzle orifice using a transparent acrylic nozzle, Int J Heat Mass Transf 143 (2019).
[14] M. Gavaises, A. Andriotis, Cavitation inside multi-hole injectors for large diesel engines and its effect on the near nozzle spray structure, SAE Technical Paper 2006-01-1114 (2006).
[15] S. Yang, Z. Ma, X. Li, D.L.S. Hung, M. Xu, A Review on the Experimental Non-intrusive Investigation of Fuel Injector Phase Changing Flow, Fuel 259 (2020).
[16] A. Sou, S. Hosokawa, A. Tomiyama, Effects of cavitation in a nozzle on liquid jet atomization, Int J Heat Mass Transf 50 (2007).
[17] M. Jeshani, Optical characterisation of cavitating flows in diesel fuel injection equipment, City University London, 2013 Ph.D. thesis.
[18] Y. Sun, Z. Guan, K. Hooman, Cavitation in diesel fuel injector nozzles and its influence on atomization and spray, Chem. Eng. Technol. 42 (2019).
[19] M. Mirshahi, J. Nouri, Y. Yan, M. Gavaises, Link between in-nozzle cavitation and jet spray in a gasoline multi-hole injector, in: ILASS-Europe, 25th European Conference on Liquid Atomization and Spray Systems, Chania, Greece, 2013.
[20] L. Lešnik, B. Kegl, G. Bombek, M. Hočevar, I. Biluš, The influence of in-nozzle cavitation on flow characteristics and spray break-up, Fuel 222 (2018).
[21] F. Payri, V. Bermúdez, R. Payri, F.J. Salvador, The influence of cavitation on the internal flow and the spray characteristics in diesel injection nozzles, Fuel 83 (2004).
[22] M. Shervani-Tabar, S. Parsa, M. Ghorbani, Numerical study on the effect of the cavitation phenomenon on the characteristics of fuel spray, Math Comput Model 56 (2012).
[23] E. Hutli, M. Nedeljkovic, A. Bonyár, D. Légrády, Experimental study on the influence of geometrical parameters on the cavitation erosion characteristics of high speed submerged jets, Exp. Therm Fluid Sci. 80 (2017).
[24] Z. Falgout, M. Linne, Cavitation inside high-Pressure optically transparent fuel injector nozzles, J. Phys. Conf. Ser. 656 (2015).
[25] J.M. Desantes, R. Payri, F.J. Salvador, J. Gimeno, Measurements of Spray Momentum for the Study of Cavitation in Diesel Injection Nozzles, SAE Technical Paper 2003-01-0007 (2003).
[26] R. Payri, J.M. García, F.J. Salvador, J. Gimeno, Using spray momentum flux measurements to understand the influence of diesel nozzle geometry on spray characteristics, Fuel 84 (2005).
[27] R. Schulz, K. Herrmann, B. von Rotz, S. Hensel, F. Seling, G. Weisser, Y. Wright, M. Bolla, K. Boulouchos, Assessing the performance of spray and combustion simulation tools against reference data obtained in a spray combustion chamber representative of large two-stroke diesel engine combustion systems, in: Proceedings of the Congress of the International Council on Combustion Engines (CIMAC), 2010.
[28] R. Schulz, S. Hensel, A. Schmid, K. Herrmann, G. Weisser, Development of spray and combustion simulation tools and application to large two-stroke diesel engine combustion systems, in: Proceedings of the Congress of the International Council on Combustion Engines (CIMAC), 2013.
[29] P.G. Aleiferis, J. Serras-Pereira, A. Augoye, T.J. Davies, R.F. Cracknell, D. Richardson, Effect of fuel temperature on in-nozzle cavitation and spray formation of liquid hydrocarbons and alcohols from a real-size optical injector for direct-injection spark-ignition engines, Int J Heat Mass Transf 53 (2010).
[30] R. Balz, A. Schmid, D. Sedarsky, In-nozzle flow investigations of marine diesel injectors, in: ILASS-Americas, 29th Annual Conference on Liquid Atomization and Spray Systems, Atlanta, GA, USA, 2017.
[31] R. Balz, D. Sedarsky, Temperature Dependent In-Nozzle Flow Investigations of Marine Diesel Injectors, in: ILASS-Americas, 30th Annual Conference on Liquid Atomization and Spray Systems, Tempe, AZ, USA, 2019.
[32] D. Schmidt, The internal flow of diesel fuel injector nozzles: areview, Int. J. Engine Res. 2 (2001).
[33] C. Arcoumanis, M. Gavaises, J. Nouri, The role of cavitation in automotive fuel injection systems, in: Proceedings of the 8th International Symposium on Internal Combustion Diagnostics, Baden-Baden, Germany, 2008.
[34] C. Wang, A. Moro, F. Xue, X. Wu, F. Luo, The influence of eccentric needle movement on internal flow and injection characteristics of a multi-hole diesel nozzle, Int J Heat Mass Transf 117 (2018).
[35] J. Zhao, W. Liu, J. Zhao, L. Grekhov, Numerical investigation of gas/liquid two-phase flow in nozzle holes considering the fuel compressibility, Int J Heat Mass Transf 147 (2020).
[36] F. Giussani, F. Piscaglia, G. Saez-Mischlich, J. Hèlie, A three-phase VOF solver for the simulation of in-nozzle cavitation effects on liquid atomization, J Comput Phys 406 (2020).
[37] D. Schmidt, S. Rakshit, K. Neroorkar, Thermal and inertial equilibrium in small, high-speed, cavitating nozzle simulations, in: ILASS-Americas, 24th Annual Conference on Liquid Atomization and Spray Systems, San Antonio, TX, USA, 2012.
[38] B. Shields, K. Neroorkar, D. Schmidt, Cavitation as rapid flash boiling, in: ILASS-Americas, 23rd Annual Conference on Liquid Atomization and Spray Systems, Ventura, CA, USA, 2011.
[39] S. Dabiri, W.A. Sirignano, D.D. Joseph, Cavitation in an orifice flow, Physics of Fluids 19 (2007).

[40] M. Bode, T. Falkenstein, M. Davidovic, H. Pitsch, H. Taniguchi, K. Murayama, T. Arima, S. Moon, J. Wang, A. Arioka, Effects of cavitation and hydraulic flip in 3-Hole GDI injectors, SAE Int. J. Fuels Lubr. 10 (2017).
[41] E.V. Berg, A. Alajbegovic, R. Tatschl, C. Krüger, U. Michels, Multiphase modeling of diesel sprays with the Eulerian/Eulerian approach, in: ILASS-Americas, 23rd Annual Conference on Liquid Atomization and Spray Systems, Zürich, Switzerland, 2001.
[42] E.V. Berg, W. Edelbauer, A. Alajbegovic, R. Tatschl, M. Vollmajer, B. Kegl, L. Ganippa, Coupled simulations of nozzle flow, primary fuel jet breakup and spray formation, J Eng Gas Turbine Power 127 (2005).
[43] M. Mithun, P. Koukouvinis, M. Gavaises, Numerical simulation of cavitation and atomization using a fully compressible three-phase model, Physics Review Fluids 3 (2018).
[44] E. Giannadakis, M. Gavaises, C. Arcoumanis, Modelling of cavitation in diesel injector nozzles, J Fluid Mech 616 (2008).
[45] M. Gavaises, F. Villa, P. Koukouvinis, M. Marengo, J.-P. Franc, Visualisation and LES simulation of cavitation cloud formation and collapse in an axisymmetric geometry, Int. J. Multiphase Flow 68 (2015).
[46] R. Marcer, P. Le Cottier, H. Chaves, B. Argueyrolles, C. Habchi, B. Barbeau, A Validated Numerical Simulation of Diesel Injector Flow Using a VOF Method, SAE Technical Paper 2000-01-2932 (2000).
[47] M. Gold, R. Pearson, J. Turner, D. Sykes, V. Stetsyuk, G. De Sercey, C. Crua, F. Koukouvinis, M. Gavaises, Simulation and measurement of transient fluid phenomena within diesel injection, SAE Technical Paper 2019-01-0066 (2019).
[48] T. Waclawczyk, T. Koronowicz, Modeling of the wave breaking with CICSAM and HRIC high resolution schemes, in: ILASS-Americas, European Conference on Computational Fluid Dynamics, Egmond aan Zee, The Netherlands, 2006.
[49] H. Zhao, S. Quan, M. Dai, E. Pomraning, P. Senecal, Q. Xue, M. Battistoni, S. Som, Validation of a three-Dimensional internal nozzle flow model including automatic mesh generation and cavitation effects, J Eng Gas Turbine Power 136 (2014).
[50] Convergent Science, Converge manual, Technical Report, 2018.
[51] K. Neroorkar, B. Shields, R. Grover, A. Torres, D. Schmidt, Application of the Homogeneous Relaxation Model to Simulating Cavitating Flow of a Diesel Fuel, SAE Technical Paper 2012-01-1269 (2012).
[52] K. Neroorkar, D. Schmidt, A Computational Investigation of Flash-boiling Multi-hole Injectors with Gasoline-ethanol blends, SAE Technical Paper 2011-01-0384 (2011).
[53] D. Schmidt, S. Gopalakrishnan, H. Jasak, Multidimensional simulation of thermal non-equilibrium channel flow, Int. J. Multiphase Flow 36 (2009).
[54] M. Battistoni, S. Som, E. Longman, Comparison of mixture and multi-Fluid models for in-Nozzle cavitation prediction, J Eng Gas Turbine Power 136 (2014).
[55] F. Brusiani, S. Negro, G. Bianchi, M. Moulai, K. Neroorkar, D. Schmidt, Comparison of the Homogeneous Relaxation Model and a Rayleigh Plesset Cavitation Model in Predicting the Cavitating Flow Through Various Injector Hole Shapes, SAE Technical Paper 2013-01-1613 (2013).
[56] F.J. Salvador, J.M. Pastor, J. De la Morena, E.C. Martínez-Miracle, Computational study on the influence of nozzle eccentricity in spray formation by means of Eulerian Σ - Y coupled simulations in diesel injection nozzles, International Journal of Multiphase Flow 129 (2020).
[57] J. Lee, R. Madabhushi, C. Fotache, S. Gopalakrishnan, D. Schmidt, Flashing flow of superheated jet fuel, Proc. Combust. Inst. 32 (2009).
[58] K. Lyras, S. Dembele, E. Vyazmina, S. Jallais, J. Wen, Numerical simulation of flash-boiling through sharp-edged orifices, International Journal of Computational Methods and Experimental Measurements 6 (2018).
[59] M. Gavaises, D. Papoulias, A. Andriotis, E. Giannadakis, Link between cavitation development and erosion damage in diesel injector nozzles, SAE Technical Paper 2007-01-0246 (2007).
[60] P. Koukouvinis, M. Gavaises, J. Li, L. Wang, Large eddy simulation of diesel injector including cavitation effects and correlation to erosion damage, Fuel 175 (2016).
[61] P. Koukouvinis, H. Naseri, M. Gavaises, Performance of turbulence and cavitation models in prediction of incipient and developed cavitation, Int. J. Engine Res. 18 (2016).
[62] W. Edelbauer, J. Strucl, A. Morozov, Large Eddy Simulation of Cavitating Throttle Flows, Advances in Hydroinformatics, Springer, 2014.
[63] Y. Gao, M. Wei, F. Yan, L. Chen, G. Li, L. Feng, Effects of cavitation flow and stagnant bubbles on the initial temporal evolution of diesel spray, Exp. Therm Fluid Sci. 87 (2017).
[64] A. Sou, B. Biçer, Numerical Simulation of Turbulent Cavitating Flow in Diesel Fuel Injector, Computers & Fluids 103 (2014).
[65] H. Weltens, H. Bressler, F. Terres, H. Neumaier, D. Rammoser, Optimisation of catalytic converter gas flow distribution by CFD prediction, SAE Technical Paper 930780 (1993).
[66] B.A. Reid, G.K. Hargrave, K.P. Garner, M.R. M., An optical comparison of the cavitation characteristics of diesel and bio-diesel blends in a true-scale nozzle geometry, Int. J. Engine Res. 14 (2013).
[67] M. Gavaises, A. Andriotis, D. Papoulias, N. Mitroglou, A. Theodorakakos, Characterization of string cavitation in large-scale Diesel nozzles with tapered holes, Physics of Fluids 25 (2009).
[68] H. Roth, M. Gavaises, C. Arcoumanis, Cavitation Initiation, its Development and Link with Flow Turbulence in Diesel Injector Nozzles, SAE Technical Paper 2002-01-0214 (2002).